DOI: 10.1002/ ((please add manuscript number))
Article type: Full Paper

Plasma-assisted growth of β-MnO_2 nanosystems as gas sensors for safety and food industry applications

Davide Barreca, Alberto Gasparotto, Filippo Gri, Elisabetta Comini, and Chiara Maccato**

Dr. D. Barreca
CNR-ICMATE and INSTM, Department of Chemical Sciences, Padova University, 35131 Padova, Italy

[*] Prof. A. Gasparotto, Dr. F. Gri, Prof. C. Maccato
Department of Chemical Sciences, Padova University and INSTM, 35131 Padova, Italy
E-mail: chiara.maccato@unipd.it

[*] Prof. E. Comini
Sensor Lab, Department of Information Engineering, Brescia University, 25133 Brescia, Italy
E-mail: elisabetta.comini@unibs.it

Keywords: β-MnO_2, plasma enhanced-chemical vapor deposition, gas sensors, acetonitrile, ethylene

Abstract: The development of efficient sensors for security field and food quality control applications has gained an ever-increasing attention for various end-uses. In this context, this work reports on the preparation of β-MnO_2 nanosystems by plasma-enhanced chemical vapor deposition (PE-CVD), using a fluorinated Mn(II) diamine-diketonate as single-source precursor for both Mn and F. Modulations of oxygen partial pressure enabled to tailor not only the morphology and oxygen vacancy content, but also fluorine doping level of the resulting systems. For the first time, the gas sensing performances of PE-CVD β-MnO_2 nanomaterials were tested in the detection of acetonitrile, a poisonous chemical warfare agent (CWA) simulant, and ethylene, an important marker of fruit ripening. The obtained results demonstrate that the fabricated sensors can efficiently detect these analytes, with the best responses at moderate temperatures (≤ 200°C), enhanced by a higher oxygen vacancy content and fluorine concentration. These features, coupled with the good selectivity and response times, candidate the developed systems as amenable platforms for practical applications.

1. Introduction

The efficient detection of chemical warfare agents (CWAs) for homeland defense and battlespace operation has received a growing attention, due to their high toxicity and dangerous effects on human health even at low concentration levels.[1-3] In this regard, sensing of acetonitrile, a simulant of cyanide CWAs[1,2,4-7] known to be itself a poisonous gas at low levels in air,[8-11] is of utmost importance to prevent health hazards.[12] In recent years, efforts have also been devoted to monitoring food quality and, in particular, fruit/vegetable ripening/degradation in horticultural industry, for which ethylene is an important marker.[5,13-20] This analyte is also a flammable gas[21,22] causing environmental problems *via* greenhouse effects.[23] On account of ubiquitous concerns regarding the target applications, the development of low-cost and reliable gas sensing materials capable of detecting the above gases in their early stages is a key issue to be still properly addressed.[24] Among the various devices for acetonitrile and ethylene detection,[17,25] chemoresistive gas sensors based on metal oxides with tailored morphology offer manifold advantages, including robustness, stability, low cost, and ease of operation.[3,4,6,21,23,26-32] So far, acetonitrile detection has been performed by SnO_2 powders,[11] films[1,2,8,10] and nanowires, along with In_2O_3 and WO_3 thin films,[4-7] $Cr_{0.8}Fe_{0.2}NbO_4$[33] and $LaCoO_3$-based films.[9] Ethylene sensing has been reported by the use of SnO_2[16,19] and WO_3 films[14,34]/powders,[15] SnO_2-WO_3 composites,[13] ZnO and WO_3 nanoparticles,[23] TiO_2-Al_2O_3 nanostructures[21] and In_2O_3 films.[22]

Among metal oxides, MnO_2, a low-cost *n*-type semiconductor,[24,35,36] exists in various polymorphs (α-, β-, γ-, δ- and ε-types) differing for the spatial linkage of octahedral MnO_6 building blocks,[24,37-43] among which rutile-type β-MnO_2 is the most stable one.[37,44,45] This structural flexibility has stimulated efforts towards MnO_2 use for various applications, from lithium batteries to supercapacitors, (photo)catalysts and amperometric sensors.[35,36,39-48] Previous studies regarding MnO_2-based gas sensors have involved the use of different

polymorphs (such as α-MnO_2 for ammonia, ethanol and hydrogen sensing,[24,27,39] β-MnO_2 for H_2, ethanol, CO[38] and acetaldehyde,[35] and δ-MnO_2 powders for hydrogen detection[37]). Further works have concerned the use of MnO_2 composites for NO_2[49] and formaldehyde detection,[26] as well as of MnO_2-coated carbon nanotubes for humidity sensors.[50] In this context, the use of MnO_2 systems, especially as supported nanomaterials, deserves further attention to overcome drawbacks associated with the use of powders[47] and enable a direct integration into sensing devices.

In previous studies, we have reported on F-doped Co_3O_4 and Fe_2O_3 nanosystems and shown that the introduction of F as a dopant resulted in improved functional properties for gas sensing and photoassisted H_2 production.[31,51,52] Inspired by these results, in this contribution we report for the first time on acetonitrile and ethylene gas sensing performances of supported β-MnO_2-based nanosystems synthesized by plasma-enhanced chemical vapor deposition (PE-CVD). In particular, the attention has been devoted to: *i)* the modulation of the systems morphology and defectivity, taking advantage of the versatility and inherent benefits offered by the above technique for low-temperature processing of inorganic nanomaterials;[53,54] *ii)* the use of $Mn(tfa)_2$•TMEDA (Htfa = 1,1,1-trifluoro-2,4-pentanedione; TMEDA = *N*,*N*,*N'*,*N'*-tetramethylethylenediamine)[55,56] as a single-source molecular precursors for both manganese and fluorine, allowing an *in-site* material doping during growth process. The rationale behind this *proof-of-concept* anionic doping lies in the possibility to boost the sensor responses and lower working temperatures, which result as attractive features in view of technological applications. After a thorough characterization of MnO_2 systems grown at different oxygen partial pressures, we have tested the sensing performances towards acetonitrile and ethylene gases, investigating the interplay between the system characteristics and important functional parameters including responses, response and recovery times, detection limits. In addition, a plausible sensing mechanism responsible for the system performances is proposed and

discussed. The results highlight favorable performances already at low operating temperatures with an enhanced detection efficiency towards the target analytes, that could provide a baseline data set for the development of MnO_2 sensors for safety and food industry applications outperforming the actual ones.

2. Results and Discussion

In the present study, two different settings of oxygen partial pressure ($p(O_2)$ = 0.06 mbar and 0.35 mbar) were adopted for the PE-CVD growth of the target samples, to investigate the effect of different oxygen contents in the used plasmas on morphology, composition, structure and gas sensing performances.

2.1. Material characterization

The system nano-organization was analyzed by field emission-scanning electron microscopy (FE-SEM). The specimen obtained at $p(O_2)$ = 0.06 mbar (Figures 1a,c) was characterized by the presence of thorn-like nanoaggregates, with average length and diameter of (700±50) nm and (70±10) nm respectively (mean aspect ratio = length/diameter= 10), protruding with a random orientation from a compact underlayer formed by interconnected spherical nanoaggregates. In a different way, for the sample grown at $p(O_2)$ = 0.35 mbar (Figures 1b,d), a highly homogeneous distribution of nanoflakes (height = (1100±100) nm; lateral dimensions = (400±40) nm; thickness = (40±5) nm), developed over a more compact layer (thickness = (200±50) nm), was detected. A possible mechanism accounting for the present system nano-organization involves the initial formation of a granular layer on the substrate surface, according to a three-dimensional growth mechanism, followed by the development of the observed anisotropic nanoaggregates.[55] This self-catalytic process is likely assisted by oxygen deficiencies (see XPS analysis below), resulting from the continuous bombardment by O-related species assisting the growth process.[53,54]

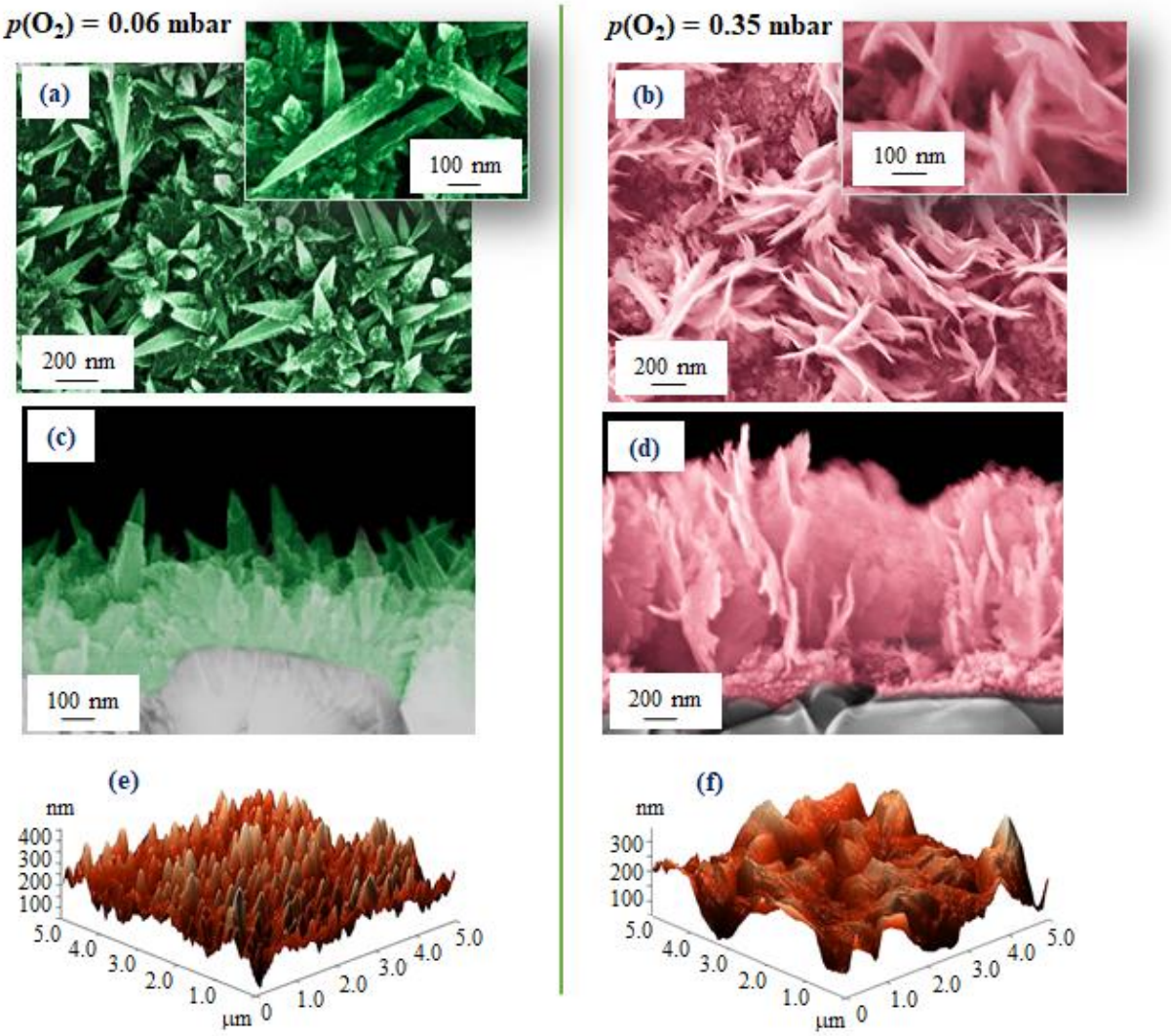

Figure 1. (a,b) Plane-view FE-SEM images, (c,d) cross-sectional FE-SEM images, and (e,f) AFM micrographs for MnO_2 specimens.

The differences between the two specimens were also reflected by atomic force microscopy (AFM) topography investigation (Figures 1e,f). For $p(O_2)$ = 0.06 mbar, an assembly of multi-grain structures could be observed (root-mean-square (RMS) roughness = 55 nm), whereas for $p(O_2)$ = 0.35 mbar no more tiny aggregates could be observed and the RMS roughness value was decreased down to 35 nm. This roughness change, directly affected by plasmochemical parameters,[52] was ascribed to the enhanced plasma bombardment at higher $p(O_2)$ values, explaining the formation of nanoflakes and the occurring morphology difference. The above roughness values, implying the obtainment of high surface-area

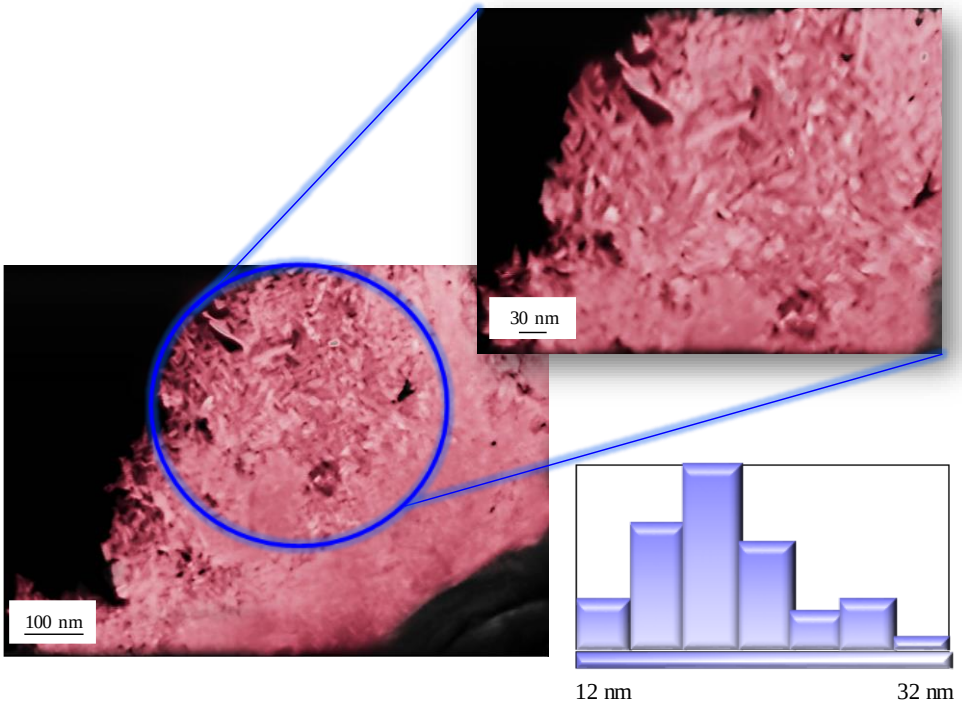

Figure 2. STEM images of sample grown at higher $p(O_2)$ along with the histogram pertaining to the crystallite size distribution.

materials especially at $p(O_2)$ = 0.06 mbar, is an attractive feature for sensing applications.[5,6,31,39] An inspection of high magnification Scanning transmission electron microscopy (STEM) images (Figure 2) evidenced that the sample prepared at $p(O_2)$ = 0.35 mbar was characterized by small crystallites (average size = 20±4 nm), resulting in the formation of nanoflakes uniformly distributed over the compact layer on Al_2O_3 substrate.

Further information was obtained by Energy dispersive X-ray spectroscopy (EDXS) compositional mapping. As observed in Figure 3a, an important feature was fluorine presence throughout the analyzed thickness, suggesting that the precursor enabled an even fluorine doping of the resulting nanodeposits (see also below). This finding, never documented in the literature so far for the target MnO_2 systems, was further corroborated by the analyses of the in-plane compositional maps (Figure 3b), that revealed a homogeneous lateral distribution of Mn, O, and F in the analyzed area, with a mean fluorine content of ≈2.0 wt. %.

To obtain a deeper insight into material composition, X-ray photoelectron spectroscopy (XPS)

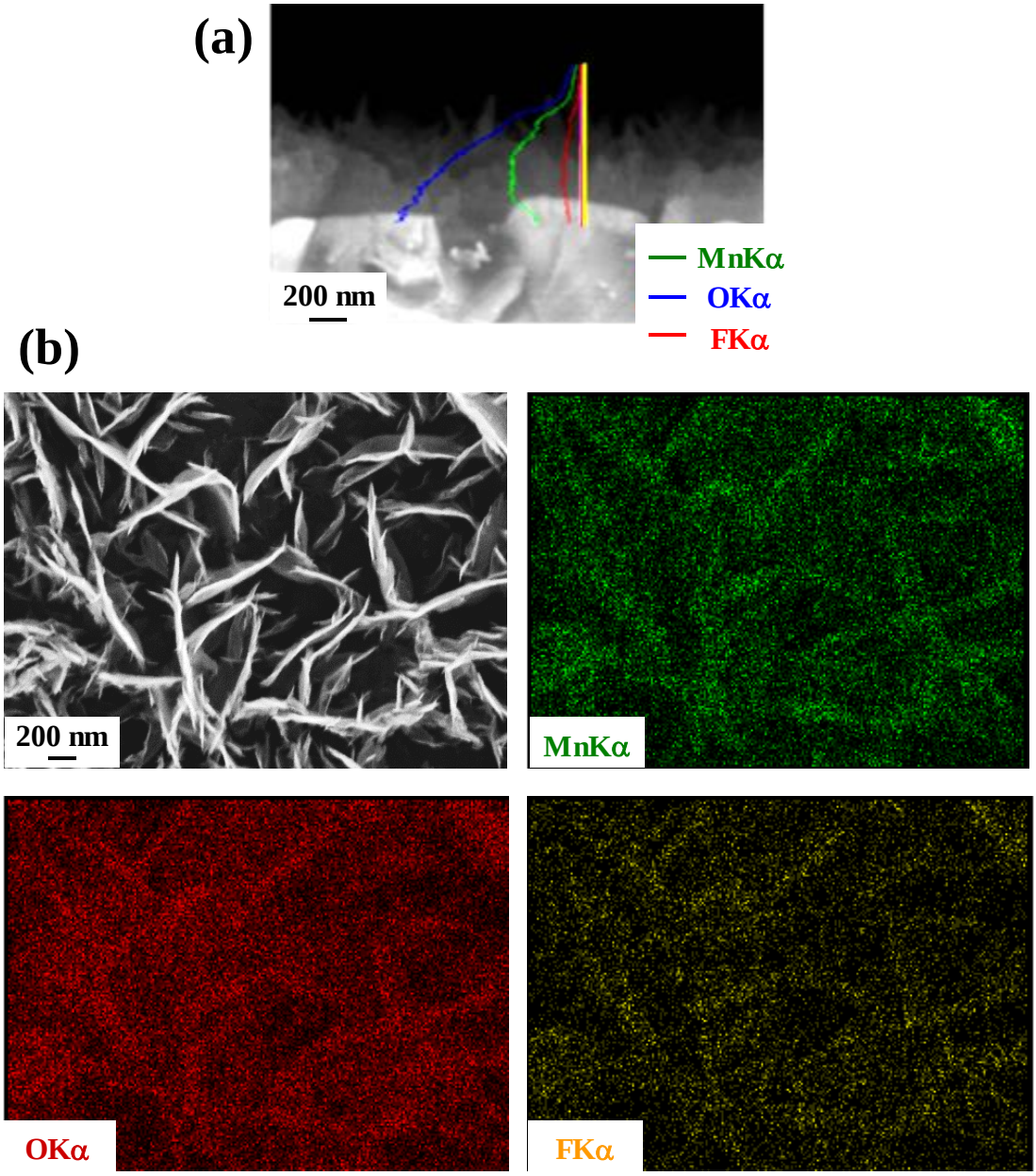

Figure 3. (a) Cross-sectional EDXS line scans for a manganese oxide specimen obtained at $p(O_2)$ = 0.06 mbar. (b) Mn Kα, O Kα and F Kα elemental maps, recorded on the corresponding FE-SEM images area, for a sample obtained at $p(O_2)$ = 0.35 mbar.

analyses were undertaken. Wide-scan spectra (Figure S1, Supporting Information), were dominated by the presence of O and Mn signals, along with a minor contribution from carbon (<10 at.%) resulting from surface contamination. As concerns the Mn2p signal (Figure 4a), its shape, binding energy (BE($Mn2p_{3/2}$) = 642.7 eV) and spin-orbit separation (11.6 eV) were in good agreement with the presence of the sole Mn(IV) oxide free from other Mn-containing

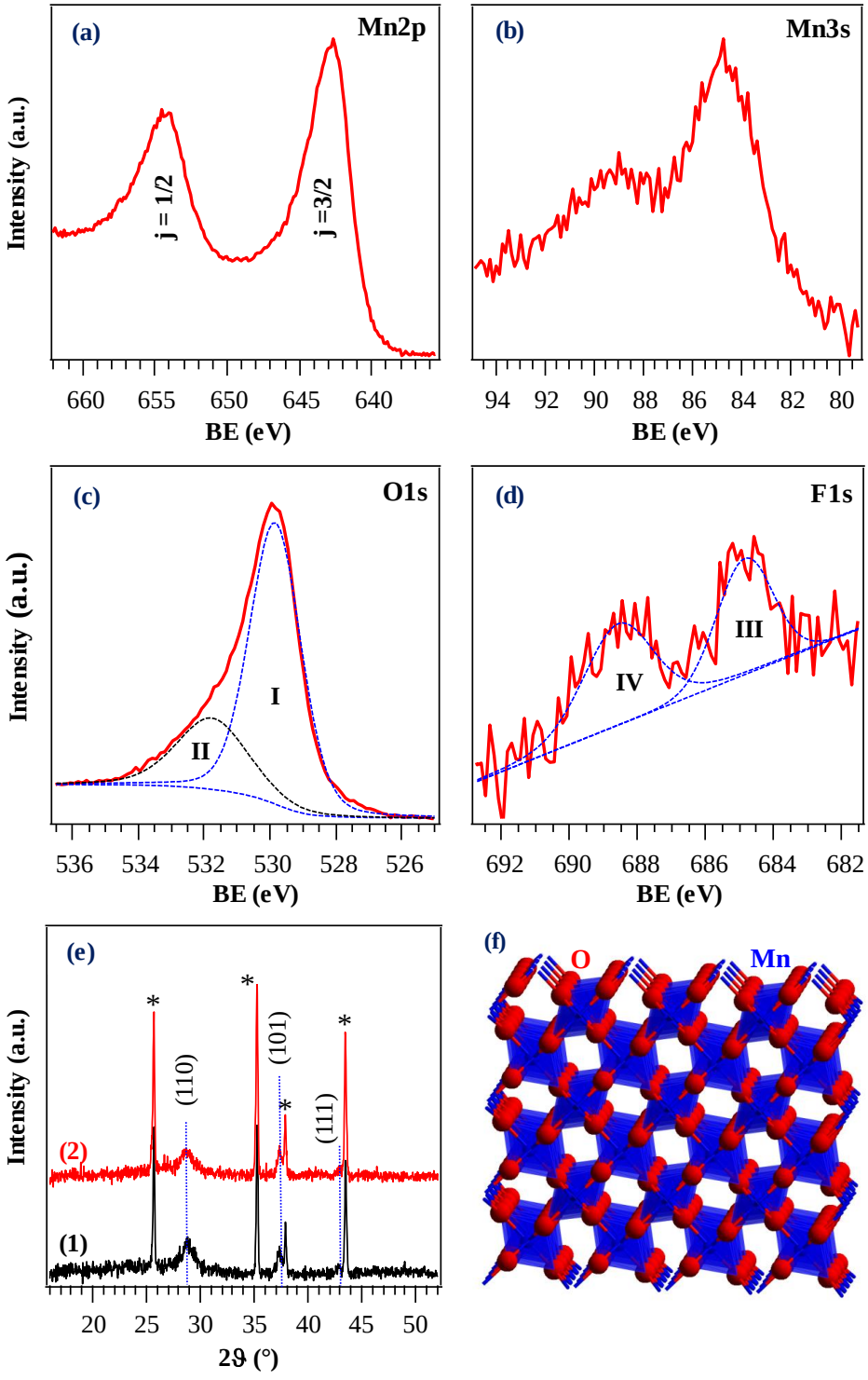

Figure 4. Surface Mn2p (a), Mn3s (b), O1s (c) and F1s (d) photopeaks for a MnO_2 specimen grown at $p(O_2)$ = 0.35 mbar. (e) X-ray diffraction (XRD) patterns of MnO_2 nanosystems grown at $p(O_2)$ = 0.06 mbar (1) and 0.35 mbar (2). Al_2O_3 substrate reflections and reference β-MnO_2 peak positions are marked by (*) and dashed lines, respectively. (f) Representation of the β-MnO_2 structure.[57]

species.[40,43,46,47,49,55] This conclusion was further corroborated by the energy difference between Mn2p$_{3/2}$ and O1s (**I**)components (112.9 eV; see also below),[24,27,37] as well as by the value of the Mn3s multiplet splitting (Figure 4b; 4.6 eV), a finger-print for Mn chemical state.[42] The O1s peak (Figure 4c) could be deconvoluted by means of two components: a main one (**I**), centered at BE = 529.8 eV, corresponding to Mn-O bonds in MnO_2 lattice, and a second lower band (**II**) at 531.8 eV, due to the concomitant contribution of –OH groups and adsorbed oxygen from atmospheric exposure.[41,46,56,58] The O/Mn atomic ratio was ≈1.6, lower than the stoichiometric value expected for MnO_2, suggesting the occurrence of oxygen vacancies.[44,45] In particular, O1s peak fitting revealed that the contribution of component (**II**) to the total oxygen content was 34.2% and 27.2% for samples obtained with $p(O_2)$ = 0.06 mbar and 0.35 mbar. In fact, considering only component **I**, O/Mn values were evaluated to be 1.07 and 1.20, respectively.

For the target specimens, two well-resolved bands contributed to the F1s signal (Figure 4d). The low BE one (**III**), centered at 684.8 eV, was traced back to the presence of lattice fluorine, due to the incorporation of F species substitutional to O sites,[31,51] confirming thus an effective fluorine doping of the obtained systems. In a different way, component (**IV**) (BE = 688.5 eV) was related to the presence of CF_x groups from precursor residuals,[31,55,59] and dropped to noise level upon a mild Ar^+ sputtering. A similar behavior was observed for carbon signals, evidencing thus the purity of the obtained nanomaterials.

The observed fluorine doping, already obtained in the PE-CVD growth of oxide nanosystems from M(hfa)$_2$•TMEDA derivatives (M = Fe, Co; Hhfa = 1,1,1,5,5,5-hexafluoro-2,4-pentanedione)[31,51,52] analogous to the present Mn(tfa)$_2$•TMEDA precursor, was traced back to the formation of F radicals during the detachment and progressive fragmentation of fluorinated diketonate moieties. These radicals, that undergo continuous collisions with the surface of the growing material under the adopted PE-CVD conditions, can account for the observed fluorine incorporation into the oxide lattice.[51] Interestingly, the level of F doping

could be tailored as a function of the adopted experimental conditions, and, in particular, lattice fluorine content was reduced from 3.5% to 1.8% upon increasing the adopted O_2 partial pressure from 0.06 to 0.35 mbar. This phenomenon could be tentatively explained taking into account that a higher O_2 content in the used plasmas is responsible for a more pronounced formation of reactive oxygen ions/radicals (O_2^+, O^-, $O^\cdot$, …).[54] The latter, in turn, likely undergo rapid reactions with the species arising from precursor fragmentation,[55] resulting in the formation of F-containing volatile byproducts and producing a less efficient fluorine incorporation in the obtained MnO_2 materials. As shown below, these differences in the system fluorine content as a function of the adopted O_2 partial pressure have a direct influence on the system sensing performances.

Taken together, XPS results confirm the formation of MnO_2, but do not enable to evidence the possible co-presence of different MnO_2 phases. In this regard, XRD patterns (Figure 4e) revealed the presence of phase-pure β-MnO_2 (*pyrolusite*;[40,57] space group: *P*42/*mnm* (136)), as confirmed by reflections at 2ϑ = 28.7°, 37.3° and by the weak shoulder at 42.8°, attributed respectively to (110), (101) and (111) planes of this tetragonal polymorph (Figure 4f).[41,57] As a matter of fact, fluorine presence did not produce any significant peak angular shift, a feature which could be traced back to the very similar ionic radii of F and O.[52] A comparison of relative peak intensities with those of the reference pattern suggested a possible (101) preferential orientation,[55] in line with the anisotropic system morphology, although the weak diffracted intensities and limited reflection number precluded more detailed information. The low average crystallite size (≈20 nm in both cases), perfectly in tune with STEM data, represents an important feature positively impacting functional properties of *n*-type chemoresistors.[16,32]

2.2. Gas sensing properties

Gas sensing performances were analyzed towards acetonitrile and ethylene, dedicating particular attention to the interplay between the system properties and the resulting functional performances.

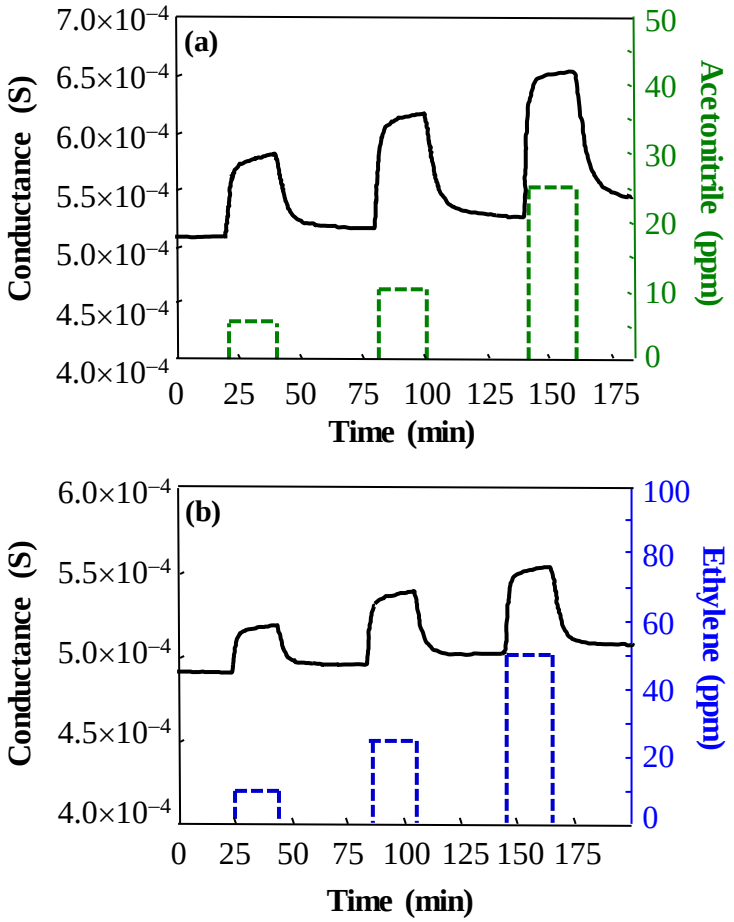

Figure 5. Isothermal dynamic responses of a β-MnO_2 specimen grown at an O_2 partial pressure $p(O_2)$ = 0.06 mbar upon exposure to concentration pulses of: (a) acetonitrile; (b) ethylene, at a working temperature of 200°C.

Figure 5 and Figure S2, Supporting Information report the dynamic responses towards square concentration pulses of the target gases. Irrespective of the analyte and the system preparation condition, injection of reducing gases resulted in a conductance increase, as expected for *n*-type oxides like β-MnO_2,[35,38,39,60] proportional to analyte concentration. No significant poisoning effects were observed for repeated exposures to acetonitrile and ethylene, and the

good baseline recovery upon purging with synthetic air after each gas pulse evidenced a good sensor stability and reversibility, of importance for practical applications.[24,31]

For an analyte concentration of 25 ppm at a working temperature of 200°C, typical response/recovery time values were 60/420 s, for ethylene, and 120/360 s for acetonitrile, respectively. The obtained recovery times were higher than the response ones, a common feature for oxide sensors ascribed to thermally activated reactions occurring at material surface.[5,31] Notably, these values were lower than the ones previously reported for CH_3CN detection by WO_3 thin films and SnO_2 films/nanowires at higher temperatures (≥450°C),[4,5] in particular the recovery times.[8,10] These issues highlight the potential of the present systems for practical applications, where fast response time are required, especially for CWAs detection.[5] Even for ethylene, the obtained values were much lower than those obtained by means of SnO_2 films[18,19] and TiO_2-Al_2O_3 systems.[21] The importance of these results is further highlighted by the fact that previous reports, for instance on In_2O_3 and WO_3-based systems, have involved the use of ethylene concentrations much higher than the present ones.[19,21,22,29]

The sensing mechanism for acetonitrile/ethylene detection by β-MnO_2 nanosystems can be explained basing on the conductance changes originated from adsorption/desorption processes upon interaction with the analytes.[24] When *n*-type β-MnO_2 systems are exposed to ambient air, O_2 chemisorption generates active oxygen species,[26,27,61,62] among which O^- is the dominant one in the adopted temperature range:[11,30]

$$O_{2\,(g)} + 2e^- \rightleftharpoons 2O^-_{(ads)} \quad (1)$$

The result is an electron capture from the outermost β-MnO_2 regions,[5] resulting in a lowered electron concentration[38] and in the formation of an electron depletion layer (see Figure 6a).[21,24,50] When acetonitrile or ethylene come in contact with β-MnO_2 nanostructures, they

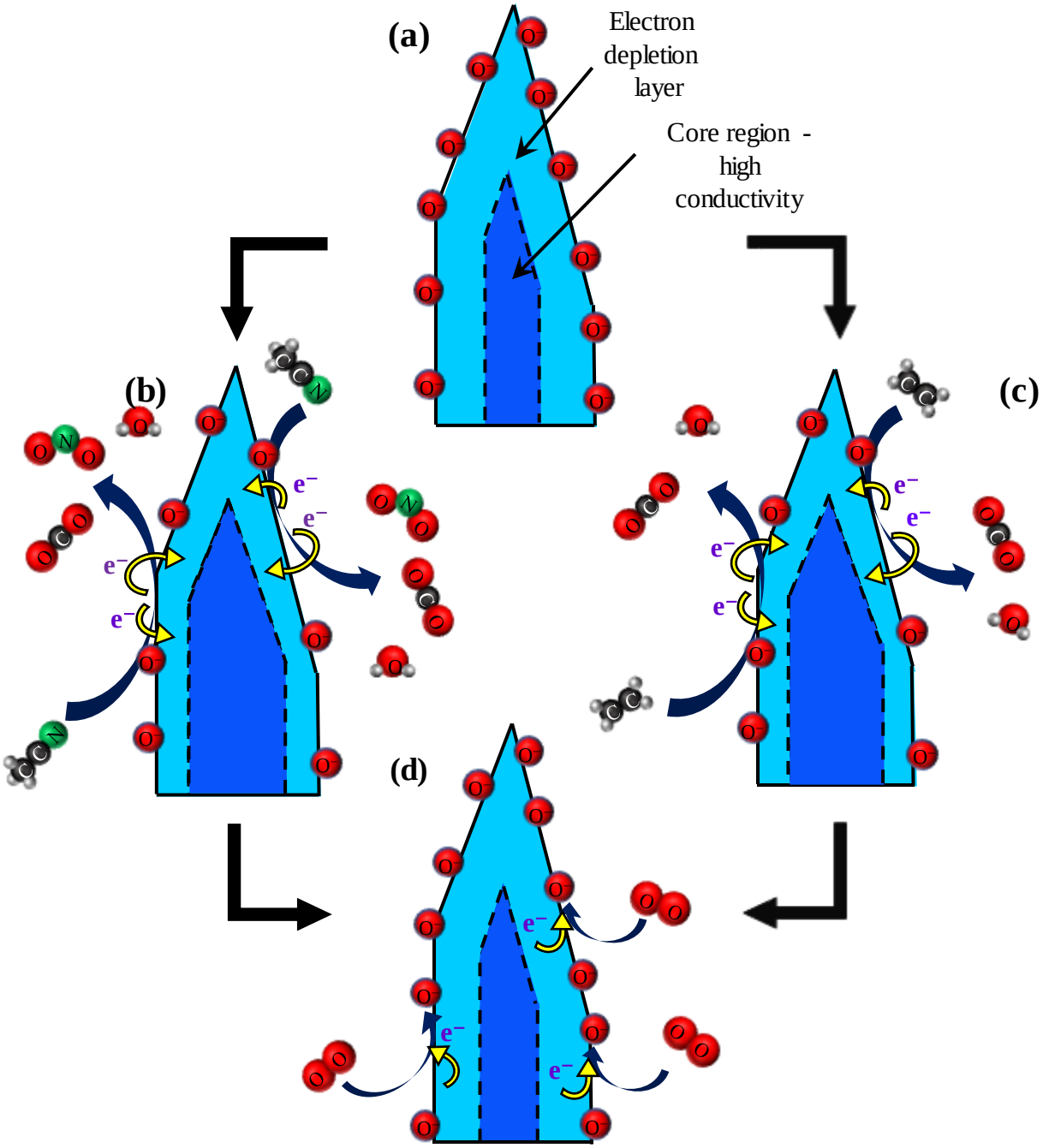

Figure 6. Sketch of the proposed gas sensing mechanism for acetonitrile and ethylene by the target *n*-type *β*-MnO_2 systems. (a) Initial air situation; chemisorption of acetonitrile (b), or ethylene (c); (d) recovery of the initial state.

react with surface adsorbed O^- species, modulating their population and thus material electrical properties:[9-11,18,19,29]

$$2CH_3CN_{(ads)} + 15O^-_{(ads)} \rightleftharpoons 4CO_{2\,(g)} + 3H_2O_{(g)} + 2NO_{2\,(g)} + 15e^- \quad (2)$$

$$C_2H_{4\,(ads)} + 6O^-_{(ads)} \rightleftharpoons 2CO_{2\,(g)} + 2H_2O_{(g)} + 6e^- \quad (3)$$

A steady state between reactions (1)-(2) or (1)-(3) determines the concentration of O^- species at the material surface, and hence conductance variations occurring upon contact with analytes. As a consequence, electrons are released back into β-MnO_2, producing a decrease in electron depletion layer thickness[50] (Figures 6b,c) and a concomitant conductance increase.[35,61] At the end of the gas pulse, no more free electrons are provided and oxygen is continuously absorbed. The initial air state is restored (Figure 6d) and therefore the conductivity decreases. This sensing behavior is strongly related to the system properties,[63] which, in turn, are appreciably influenced by the synthesis conditions (see also below).

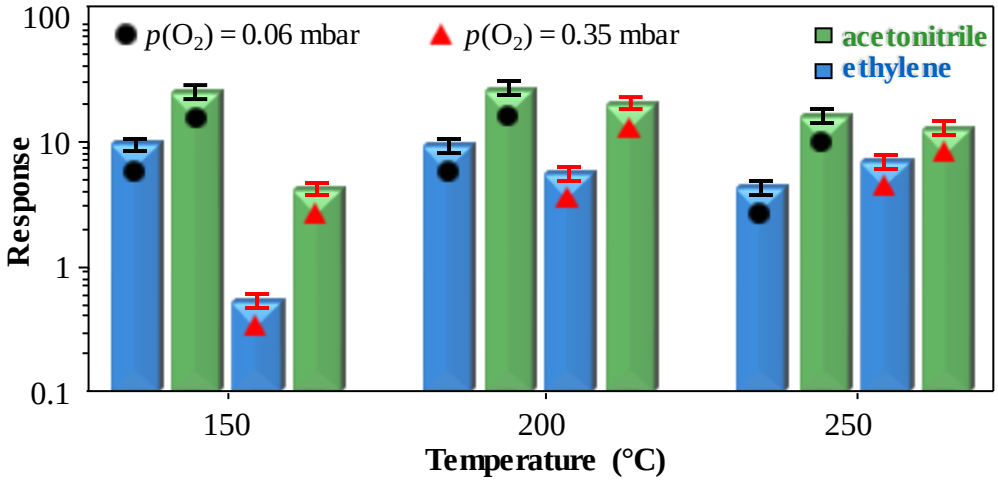

Figure 7. Responses as a function of the adopted operating temperature towards 25 ppm of acetonitrile and ethylene for β-MnO_2 nanosystems grown at different $p(O_2)$. The response is defined as the relative conductance variation upon contact with the analytes (see equation (4)).

Figure 7 displays responses to acetonitrile and ethylene for β-MnO_2 specimens synthesized at $p(O_2)$ = 0.06 and 0.35 mbar as a function of the adopted working temperature. As can be observed, acetonitrile responses were systematically higher than ethylene ones, due to the higher number of electrons released in reaction (2) with respect to reaction (3). In general, the response dependence on the operating temperature was directly dependent on both the

adopted analyte and the used specimen. As regards the sample synthesized at $p(O_2)$ = 0.06 mbar, for both analytes responses remained almost constant upon going from 150 to 200°C, whereas they decreased at 250°C. This phenomenon, in line with literature data for ethylene[13] and acetonitrile[9,19] detection, suggested that at higher temperatures the decrease in analyte adsorption on material surface was not adequately compensated by the increased extent of surface reaction.[24,63] Furthermore, higher temperatures promote CH_3CN decomposition, resulting in a higher amount of surface CN^- by capture of released electrons and in a concomitant response reduction.[11]

Conversely, as concerns the specimen obtained at $p(O_2)$ = 0.35 mbar, the response to ethylene increased with the working temperature, whereas the response to acetonitrile was maximum at 200°C. Regarding ethylene, such a behavior could be explained considering that a progressive increase in operating temperature enabled to overcome the process activation energy barrier (reaction (3)), producing the observed response enhancement.[27,28,63] A similar observation held even for CH_3CN at temperatures <200°C, whereas in this case, for higher temperatures, the decreased analyte adsorption produced a response decrease.[5,49,63]

Remarkably, the best response values obtained in this work are higher than those reported for acetonitrile detection by In_2O_3 films/nanowires,[6] SnO_2 and WO_3 films at analogous,[5] or even higher,[2,7,10] temperatures, and $LaCoO_3$-based systems.[9] Even for ethylene, previously reported response values for its detection by ZnO, SnO_2, WO_3 and SnO_2-WO_3 sensors, as well as carbon nanotube-based devices,[20] were inferior.[13,14,16,29] It is also worth highlighting that, differently from the present study, ethylene and acetonitrile detection are typically carried out at temperatures ≥ 300-350°C,[4,5,7,14-16,19,29] since low response signals were obtained under milder conditions.

The very good performances of the present sensors are the outcome of various factors, which include their morphology, defect content and fluorine doping level. The former, implying a

very favorable high surface-to-volume ratio,[27,28] was likely responsible for the relatively high content of oxygen vacancies, that contribute to the favorable β-MnO_2 catalytic properties.[44,45] These defects result in a higher chemical reactivity and an enhanced gas uptake with respect to conventional systems.[32,40,63,64] A further beneficial contribution is provided by fluorine incorporation into β-MnO_2 lattice (see EDXS and XPS results). In fact, due to the high electronegativity, F centers withdraw electron density from the bonded Mn ones, enhancing their Lewis acidity and the resulting catalytic activity. In addition, F presence passivates defects acting as charge carrier recombination centers, increasing thus available electron concentration and promoting an enhanced detection efficiency.[31]

The different morphology, defect content and fluorine doping level are indeed the key parameters accounting for the different functional behavior of systems synthesized at $p(O_2)$ = 0.06 and 0.35 mbar. In fact, a detailed inspection of data reported in Figures 7 and 8 revealed that the β-MnO_2 sample synthesized at an oxygen partial pressure of 0.06 mbar always yielded superior responses than the homologous prepared at $p(O_2)$ = 0.35 mbar, and that, in the former case, the highest responses were registered at lower working temperatures. This downward shift of the best sensing temperature is of key interest to reduce power consumption and enhance the sensor suitability for the target technological end uses.[31] The present behavior indicated a change in the sensing pattern for the two systems, which could be explained taking into account that the best performing system prepared at $p(O_2)$ = 0.06 mbar possessed: i) a higher RMS roughness value, implying a higher active area for the interaction with the target gases; ii) a higher defect content, as evidenced by XPS analyses, and iii) a higher fluorine doping level, exerting a beneficial effect on the system functional properties (see above).

The obtained responses were also investigated as a function of acetonitrile and ethylene concentrations. The linear trends in the log-log scale (Figures 8a,b) confirmed the absence of

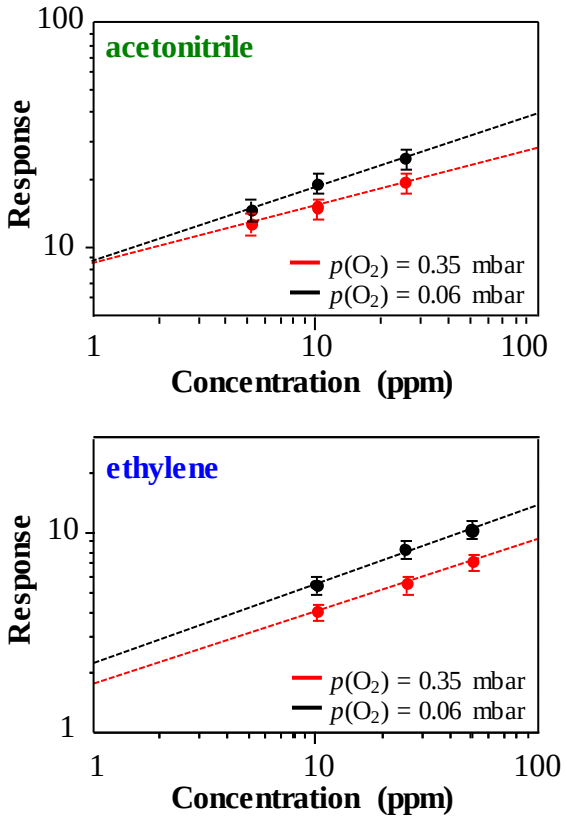

Figure 8. Responses of the target β-MnO_2 nanosystems *vs*. acetonitrile and ethylene concentration at a fixed working temperature of 200°C. The response is defined as the relative conductance variation upon contact with the analytes (see equation (4)).

saturation phenomena and indicated that these gases can be quantitatively detected,[22] an important issue for eventual practical applications.[39] Conversely, previous results on acetonitrile and ethylene sensing by SnO_2 films have shown response saturation at increasing analyte concentrations.[1,2,8,10,16]

At 200°C, the optimal operating temperature, the best detection limits, obtained for the sample grown at $p(O_2)$ = 0.06 mbar, were 0.05 and 1.9 ppm for acetonitrile and ethylene, respectively. Remarkably, the value for acetonitrile was significantly lower than the pertaining cyanide compounds IDLH (immediately dangerous for life band health) threshold (a few tenths of ppm).[4-7] For ethylene, the obtained detection limit, comparing favorably with previous results,[34] was of the same order of magnitude of the minimum concentration triggering the ripening process in fruits/vegetables[13,15,17,20] and of the threshold limit value

(TLV), *i.e.* the maximum concentration allowed for repeated exposure without adverse health effects.[23] In addition, our value was appreciably inferior to ethylene explosion limit in air (35000 ppm),[22] enabling to successfully extend the application of the present systems even to safety end-uses.

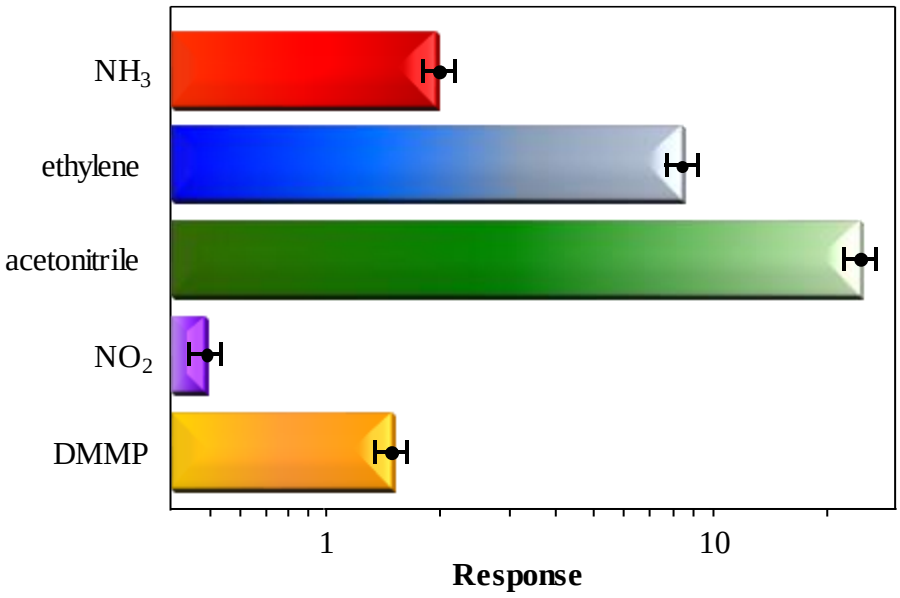

Figure 9. Responses of a β-MnO_2 specimen grown at $p(O_2)$ = 0.06 mbar towards NH_3 (10 ppm), ethylene (25 ppm), acetonitrile (25 ppm), NO_2 (2 ppm) and DMMP (5 ppm). Working temperature = 200°C.

In general, the ubiquitous metal oxide cross-sensitivity towards different analytes may generate false alarm in the detection process,[33] and the sensor selectivity is a key concern especially under real-world conditions.[33] To test possible false alarms, we used NO_2, a highly toxic pollutant,[30,49,64] NH_3, an irritating chemical largely occurring in industrial and medical environments,[33] and dimethyl methyl phosphonate (DMMP), a simulant for another CWA, Sarin nerve agent.[1,3,4,7,30] In this regard, Figure 9 reports a general overview of response values to selected concentrations of various analytes for the best performing system targeted in the present study. As can be observed, very weak responses to DMMP, NH_3 and NO_2 were obtained, in line with previous results on ammonia and nitrogen dioxide detection by MnO_2-based systems.[24,27,49] The data highlighted an improved detection efficiency of β-

MnO_2 sensors towards acetonitrile and ethylene, an important issue considering that other oxide-based sensors are scarcely selective to these analytes in the presence of interfering gases.[21,29,33,34] The present results are of potential interest in view of real-time gas monitoring equipments,[37] either for safety or food industry applications.

3. Conclusion

This study has reported on the plasma-assisted synthesis of F-doped β-MnO_2 nanosystems. The target materials were grown on polycrystalline alumina substrates starting from a fluorinated Mn(II) diamine-diketonate molecular source in Ar-O_2 plasmas. Under the adopted conditions, the above compound acted as a single-source precursor for both manganese and fluorine, enabling the obtainment of phase-pure β-MnO_2 nanomaterials doped with fluorine, an unprecedented result for MnO_2 systems. The developed systems were adopted for the fabrication of chemoresistive gas sensors, which exhibited appreciable responses and a good selectivity towards acetonitrile and ethylene, used as hazardous analytes/CWA simulants and probes for fruit ripening, respectively. The sensor responses were favorably influenced by the system morphology, oxygen vacancy content and fluorine content in the developed materials, that could be tailored by variations of the sole oxygen partial pressure. The pronounced detection efficiency even in the presence of interferents, coupled with good response times and system stability, candidate the developed sensors for the eventual detection of both analytes with a decreased energy consumption, paving the way to possible real-world safety and food industry applications. These preliminary results may act as a pointer to address the potential of Mn oxide-based systems for the target applications, meeting the demands of a variety of end-uses through subsequent performance mastering.

4. Experimental Section

Plasma-assisted chemical vapor deposition: In this work, PE-CVD growth experiments were

performed using $Mn(tfa)_2$•TMEDA[55,56] as precursor. Depositions were carried out by means of a two-electrode PE-CVD apparatus[54] with by a Radio Frequency (RF, ν = 13.56 MHz) generator. Prior to each experiment, polycrystalline Al_2O_3 substrates (thickness = 254 μm) were subjected to a cleaning procedure involving sonication in dichloromethane and in 2-propanol, and mounted on the grounded electrode. Electronic grade Ar and O_2 were used as plasma sources. The precursor powders were placed in an external vessel heated at 85°C, and the vapors were transported towards the deposition zone by an Ar flow (rate = 60 standard cubic centimeters per minute (sccm)) through gas lines heated at 150°C. Additional Ar (15 sccm) and O_2 flows (rates = 5 and 40 sccm, corresponding to oxygen partial pressures $p(O_2)$ = 0.06 mbar and 0.35 mbar, respectively) were separately introduced into the reactor. For all depositions the total pressure, duration, RF-power, substrate temperature and interelectrode distance were kept at 1.0 mbar, 1 h, 20 W, 300°C and 6 cm, respectively.

Material characterization: FE-SEM analyses were carried out by a Zeiss SUPRA 40 VP instrument at beam voltage between 5.0 and 10.0 kV. STEM images were collected on the same instrument using an acceleration voltage of 20.0 kV. The ImageJ® (http://imagej.nih.gov/ij/, accessed September 2017) picture analyzer software was used to estimate the average grain size and deposit thickness. EDXS analyses were performed on the same instrument using an Oxford INCA x-sight X-ray detector, using a beam voltage of 20.0 kV.

AFM analysis was performed by an NT-MDT SPM solver P47H-PRO instrument, operating in tapping mode. RMS roughness values were evaluated on 5×5 μm^2 images after background subtraction and plane fitting.

XPS measurements were performed on a Perkin-Elmer Φ 5600ci spectrometer using a standard AlKα radiation (1486.6 eV). Binding energies (BEs; uncertainty = ±0.2 eV) were corrected for charging by assigning a BE of 284.8 eV to the adventitious C1s peak. The analysis involved Shirley-type background subtraction and, when necessary, spectral

deconvolution by non-linear least-squares fitting adopting Gaussian-Lorentzian functions. Atomic percentages were calculated using (Φ V5.4A software sensitivity factors). Ar^+ sputtering was carried out at 4.0 kV (Ar partial pressure = 5×10^{-8} mbar).

XRD patterns were collected in glancing incidence mode (incidence angle = 1.0°) by a Bruker D8 Advance diffractometer equipped with a Göbel mirror, using a CuKα source. The average crystallite dimensions were estimated using the Scherrer equation.[20,35,61]

Gas sensing experiments: Gas sensing analyses were performed by measuring resistance transients as a function of temperature and gas concentration pulses. To fabricate the sensing devices, material deposition was performed on Al_2O_3 transducers (size = 3×3 mm^2), and subsequently Pt interdigitated contacts and a Pt heater were deposited by sputtering on the sensing material and on the Al_2O_3 backside, respectively. Analyses were performed in a stabilized sealed chamber (relative humidity = 40% at 20°C) at working temperatures <300°C, in order to avoid undesired transformations of MnO_2 into other Mn oxides.[36] Before testing, samples were stabilized at each working temperature for 8 h. A synthetic air flow (rate = 300 sccm) at atmospheric pressure was used as carrier for the dispersion of analytes. Different gas concentrations were obtained by mass flow controllers, mixing fluxes from gas sources, dry air bottles, and saturated wet air source.[6] Conductance values were obtained measuring the current flowing through MnO_2 deposits upon application of a constant voltage (1 V).

The sensor response was evaluated as:[28,35,61]

$$\text{Response} = (G_g - G_a)\times100 / G_a = (\Delta G / G_a)\times100 \quad (4)$$

where G_a and G_g indicate the baseline conductance in air and the steady state value reached after gas exposure. Repeated measurements under the same conditions after one day, one month and six months yielded stable responses (maximum uncertainty = 10%), an essential parameters from the viewpoint of practical application.[21,24]

Response data *vs*. analyte concentration were fitted by the relation:[27]

$$\text{Response (\%)} = K \times C^X \quad (5)$$

where K is a constant, C is the analyte concentration and X is an exponent dependent on the charge of surface species[29] and the stoichiometry of involved elementary reactions.[60] Assuming the validity of equation (5) even for low analyte concentrations, detection limits were extrapolated. The response time was estimated as the time required for conductance to reach 90% of the difference between steady state and air values,[4,23,62] whereas the recovery time was the one necessary to return to 70% of the original conductance in air after gas injection has been shut off.[7,63] In both cases, maximum uncertainty was estimated to be 10%.

Supporting Information
Supporting Information is available from the Wiley Online Library or from the author.

Acknowledgements

This work was financially supported by funding from Padova University DOR 2016–2017 and P-DiSC #03BIRD2016-UNIPD projects. Special thanks are also due to Dr. G. Carraro (Department of Chemical Sciences, Padova University, Italy) for skilful experimental assistance.

Received: ((will be filled in by the editorial staff))
Revised: ((will be filled in by the editorial staff))
Published online: ((will be filled in by the editorial staff))

References

[1] S. C. Lee, S. Y. Kim, W. S. Lee, S. Y. Jung, B. W. Hwang, D. Ragupathy, D. D. Lee, S. Y. Lee, J. C. Kim, *Sensors* **2011**, *11*, 6893.

[2] W. S. Lee, S. C. Lee, S. J. Lee, D. D. Lee, J. S. Huh, H. K. Jun, J. C. Kim, *Sens. Actuators, B* **2005**, *108*, 148.

[3] R. Yoo, S. Yoo, D. Lee, J. Kim, S. Cho, W. Lee, *Sens. Actuators, B* **2017**, *240*, 1099.

[4] E. Comini, C. Baratto, I. Concina, G. Faglia, M. Falasconi, M. Ferroni, V. Galstyan, E. Gobbi, A. Ponzoni, A. Vomiero, D. Zappa, V. Sberveglieri, G. Sberveglieri, *Sens. Actuators, B* **2013**, *179*, 3.

[5] A. Ponzoni, E. Comini, I. Concina, M. Ferroni, M. Falasconi, E. Gobbi, V. Sberveglieri, G. Sberveglieri, *Sensors* **2012**, *12*, 17023.

[6] A. Ponzoni, C. Baratto, S. Bianchi, E. Comini, M. Ferroni, M. Pardo, M. Vezzoli, A. Vomiero, G. Faglia, G. Sberveglieri, *IEEE Sens. J.* **2008**, *8*, 735.

[7] G. Sberveglieri, C. Baratto, E. Comini, G. Faglia, M. Ferroni, M. Pardo, A. Ponzoni, A. Vomiero, *Thin Solid Films* **2009**, *517*, 6156.

[8] J. R. Sohn, H. D. Park, D. D. Lee, *J. Catal.* **2000**, *195*, 12.

[9] A. V. Salker, D. D. Lee, *Sens. Lett.* **2007**, *5*, 416.

[10] J. R. Sohn, H. D. Park, D. D. Lee, *Appl. Surf. Sci.* **2000**, *161*, 78.

[11] M. J. Lee, H. W. Cheong, L. D. N. Son, Y. S. Yoon, *Jpn. J. Appl. Phys.* **2008**, *47*, 2119.

[12] Y. Sun, K. Y. Ong, *Detection technologies for chemical warfare agents and toxic vapours*, CRC Press, Boca Raton, USA, 2005.

[13] Y. Pimtong-Ngam, S. Jiemsirilers, S. Supothina, *Sens. Actuators, A* **2007**, *139*, 7.

[14] P. Ivanov, E. Llobet, A. Vergara, M. Stankova, X. Vilanova, J. Hubalek, I. Gracia, C. Cané, X. Correig, *Sens. Actuators, B* **2005**, *111-112*, 63.

[15] O.-u. Nimittrakoolchai, S. Supothina, *Mater. Chem. Phys.* **2008**, *112*, 270.

[16] D. Jadsadapattarakul, C. Thanachayanont, J. Nukeaw, T. Sooknoi, *Sens. Actuators, B* **2010**, *144*, 73.

[17] N. A. Zaidi, M. W. Tahir, M. J. Vellekoop, W. Lang, *Sensors* **2017**, *17*, 2283.

[18] M. Agarwal, M. D. Balachandran, S. Shrestha, K. Varahramyan, *J. Nanomater.* **2012**, *2012*, 145406.

[19] H. Ahn, J. H. Noh, S.-B. Kim, R. A. Overfelt, Y. S. Yoon, D.-J. Kim, *Mater. Chem. Phys.* **2010**, *124*, 563.

[20] B. Esser, J. M. Schnorr, T. M. Swager, *Angew. Chem. Int. Ed.* **2012**, *51*, 5752.

[21] M. M. Arafat, A. S. M. A. Haseeb, S. A. Akbar, M. Z. Quadir, *Sens. Actuators, B* **2017**, *238*, 972.

[22] Y. Cao, J. Zhao, X. Zou, P.-P. Jin, H. Chen, R. Gao, L.-J. Zhou, Y.-C. Zou, G.-D. Li, *RSC Adv.* **2015**, *5*, 5424.

[23] T. Samerjai, N. Tamaekong, K. Wetchakun, V. Kruefu, C. Liewhiran, C. Siriwong, A. Wisitsoraat, S. Phanichphat, *Sens. Actuators, B* **2012**, *171-172*, 43.

[24] C. Liu, S. T. Navale, Z. B. Yang, M. Galluzzi, V. B. Patil, P. J. Cao, R. S. Mane, F. J. Stadler, *J. Alloys Compd.* **2017**, *727*, 362.

[25] R. Zhang, M.-I. Tejedor, M. A. Anderson, M. Paulose, C. A. Grimes, *Sensors* **2002**, *2*, 331.

[26] C. Xie, L. Xiao, M. Hu, Z. Bai, X. Xia, D. Zeng, *Sens. Actuators, B* **2010**, *145*, 457.

[27] A. Sanger, A. Kumar, A. Kumar, R. Chandra, *Sens. Actuators, B* **2016**, *234*, 8.

[28] A. K. Srinath, L. Sankaranarayanan, R. Pandeeswari, B. G. Jeyaprakash, *Microchim. Acta* **2015**, *182*, 1619.

[29] E. Wongrat, N. Chanlek, C. Chueaiarrom, W. Thupthimchun, B. Samransuksamer, S. Choopun, *Ceram. Int.* **2017**, *43*, S557.

[30] E. Comini, *Anal. Chim. Acta* **2006**, *568*, 28.

[31] D. Barreca, D. Bekermann, E. Comini, A. Devi, R. A. Fischer, A. Gasparotto, M. Gavagnin, C. Maccato, C. Sada, G. Sberveglieri, E. Tondello, *Sens. Actuators, B* **2011**, *160*, 79.

[32] J. Zhang, Z. Y. Qin, D. W. Zeng, C. S. Xie, *Phys. Chem. Chem. Phys.* **2017**, *19*, 6313.

[33] A. Sree Rama Murthy, D. Pathak, G. Sharma, K. I. Gnanasekar, V. Jayaraman, A. M. Umarji, T. Gnanasekaran, *Anal. Chim. Acta* **2015**, *892*, 175.

[34] F. Caprioli, L. Quercia, *Sens. Actuators, B* **2014**, *203*, 187.

[35] S. Balamurugan, A. Rajalakshmi, D. Balamurugan, *J. Alloys Compd.* **2015**, *650*, 863.

[36] M.-K. Song, S. Cheng, H. Chen, W. Qin, K.-W. Nam, S. Xu, X.-Q. Yang, A. Bongiorno, J. Lee, J. Bai, T. A. Tyson, J. Cho, M. Liu, *Nano Lett.* **2012**, *12*, 3483.

[37] X. Q. Tian, L. Yang, X. X. Qing, K. Yu, X. F. Wang, *Sens. Actuators, B* **2015**, *207*, 34.

[38] J. Xiao, P. Liu, Y. Liang, H. B. Li, G. W. Yang, *J. Appl. Phys.* **2013**, *114*, 073513.

[39] W. X. Zhang, C. Y. Zeng, M. Kong, Y. M. Pan, Z. H. Yang, *Sens. Actuators, B* **2012**, *162*, 292.

[40] B. Y. Bai, J. H. Li, J. M. Hao, *Appl. Catal., B* **2015**, *164*, 241.

[41] C. Revathi, R. T. R. Kumar, *Electroanalysis* **2017**, *29*, 1481.

[42] O. Nilsen, H. Fjellvåg, A. Kjekshus, *Thin Solid Films* **2003**, *444*, 44.

[43] Y. Liu, Z. Zeng, B. Bloom, D. H. Waldeck, J. Wei, *Small* **2018**, *14*, 1703237.

[44] J. A. Dawson, I. Tanaka, *ACS Appl. Mater. Interfaces* **2014**, *6*, 17776.

[45] J. Xu, J. B. Liu, B. Huang, S. N. Li, B. X. Liu, *Acta Mater.* **2017**, *131*, 88.

[46] J. M. Li, Z. P. Qu, Y. Qin, H. Wang, *Appl. Surf. Sci.* **2016**, *385*, 234.

[47] A. Ramírez, P. Hillebrand, D. Stellmach, M. M. May, P. Bogdanoff, S. Fiechter, *J. Phys. Chem. C* **2014**, *118*, 14073.

[48] B. Wu, G. Zhang, M. Yan, T. Xiong, P. He, L. He, X. Xu, L. Mai, *Small* **2018**, *14*, 1703850.

[49] C. Zhang, A. Boudiba, C. Navio, M.-G. Olivier, R. Snyders, M. Debliquy, *Sens. Actuators, B* **2012**, *161*, 914.

[50] D. Jung, J. Kim, G. S. Lee, *Sens. Actuators, A* **2015**, *223*, 11.

[51] A. Gasparotto, D. Barreca, D. Bekermann, A. Devi, R. A. Fischer, P. Fornasiero, V. Gombac, O. I. Lebedev, C. Maccato, T. Montini, G. Van Tendeloo, E. Tondello, *J. Am. Chem. Soc.* **2011**, *133*, 19362.

[52] G. Carraro, D. Barreca, D. Bekermann, T. Montini, A. Gasparotto, V. Gombac, C. Maccato, P. Fornasiero, *J. Nanosci. Nanotechnol.* **2013**, *13*, 4962.

[53] J. Zheng, R. Yang, L. Xie, J. Qu, Y. Liu, X. Li, *Adv. Mater.* **2010**, *22*, 1451.

[54] D. Barreca, A. Gasparotto, E. Tondello, C. Sada, S. Polizzi, A. Benedetti, *Chem. Vap. Deposition* **2003**, *9*, 199.

[55] D. Barreca, G. Carraro, E. Fois, A. Gasparotto, F. Gri, R. Seraglia, M. Wilken, A. Venzo, A. Devi, G. Tabacchi, C. Maccato, *J. Phys. Chem. C* **2018**, *122*, 1367.

[56] C. Maccato, L. Bigiani, G. Carraro, A. Gasparotto, R. Seraglia, J. Kim, A. Devi, G. Tabacchi, E. Fois, G. Pace, V. Di Noto, D. Barreca, *Chem. Eur. J.* **2017**, *23*, 17954.

[57] Pattern No. 024-0735, JCPDS (2000)

[58] Z.-S. Wu, W. Ren, D.-W. Wang, F. Li, B. Liu, H.-M. Cheng, *ACS Nano* **2010**, *4*, 5835.

[59] http://srdata.nist.gov/xps

[60] M. Epifani, E. Comini, P. Siciliano, G. Faglia, J. R. Morante, *Sens. Actuators, B* **2015**, *217*, 193.

[61] S. Fairose, S. Ernest, Ashna, *Mater. Today: Proc.* **2017**, *4*, 12085.

[62] F. Qu, Y. Yuan, R. Guarecuco, M. Yang, *Small* **2016**, *12*, 3128.

[63] D. Barreca, D. Bekermann, E. Comini, A. Devi, R. A. Fischer, A. Gasparotto, C. Maccato, G. Sberveglieri, E. Tondello, *Sens. Actuators, B* **2010**, *149*, 1.

[64] Y. Li, B. Zu, Y. Guo, K. Li, H. Zeng, X. Dou, *Small* **2016**, *12*, 1420.